AGU PUBLICATIONS

JGR

Journal of Geophysical Research: Space Physics

RESEARCH ARTICLE
10.1002/2017JA024913

Special Section:
Mars Aeronomy

Ionospheric Irregularities at Mars Probed by MARSIS Topside Sounding

Y. Harada[1], D. A. Gurnett[1], A. J. Kopf[1], J. S. Halekas[1], and S. Ruhunusiri[1]

[1]Department of Physics and Astronomy, University of Iowa, Iowa City, IA, USA

Key Points:
- MARSIS observes diffuse ionospheric echoes, which are indicative of ionospheric irregularities around the exobase at Mars
- The winter hemisphere and high solar zenith angles are strongly favored for observations of the diffuse echoes
- The ionospheric irregularities are driven primarily by atmospheric gravity waves and secondarily by solar wind forcing

Correspondence to:
Y. Harada,
yuki-harada@uiowa.edu

Citation:
Harada, Y., Gurnett, D. A., Kopf, A. J., Halekas, J. S., & Ruhunusiri, S. (2018). Ionospheric irregularities at Mars probed by MARSIS topside sounding. *Journal of Geophysical Research: Space Physics*, *123*, 1018–1030. https://doi.org/10.1002/2017JA024913

Received 20 OCT 2017
Accepted 15 JAN 2018
Accepted article online 18 JAN 2018
Published online 30 JAN 2018

Abstract The upper ionosphere of Mars contains a variety of perturbations driven by solar wind forcing from above and upward propagating atmospheric waves from below. Here we explore the global distribution and variability of ionospheric irregularities around the exobase at Mars by analyzing topside sounding data from the Mars Advanced Radar for Subsurface and Ionosphere Sounding (MARSIS) instrument on board Mars Express. As irregular structure gives rise to off-vertical echoes with excess propagation time, the diffuseness of ionospheric echo traces can be used as a diagnostic tool for perturbed reflection surfaces. The observed properties of diffuse echoes above unmagnetized regions suggest that ionospheric irregularities with horizontal wavelengths of tens to hundreds of kilometers are particularly enhanced in the winter hemisphere and at high solar zenith angles. Given the known inverse dependence of neutral gravity wave amplitudes on the background atmospheric temperature, the ionospheric irregularities probed by MARSIS are most likely associated with plasma perturbations driven by atmospheric gravity waves. Though extreme events with unusually diffuse echoes are more frequently observed for high solar wind dynamic pressures during some time intervals, the vast majority of the diffuse echo events are unaffected by varying solar wind conditions, implying limited influence of solar wind forcing on the generation of ionospheric irregularities. Combination of remote and in situ measurements of ionospheric irregularities would offer the opportunity for a better understanding of the ionospheric dynamics at Mars.

1. Introduction

The dayside ionosphere of Mars is created primarily by photoionization of the neutral atmosphere by solar extreme ultraviolet radiation. Though the primary portion of the Martian ionosphere is well described by a Chapman layer, a wealth of observations indicate the presence of complex structure and dynamics that are not predicted by Chapman theory (Withers, 2009, and references therein). For example, as a consequence of the absence of a strong global magnetic field, the upper atmosphere of Mars directly interacts with the solar wind, driving a variety of dynamic processes in the upper ionosphere (e.g., Dubinin et al., 2008, 2009; Gurnett et al., 2010; Halekas, Brain, et al., 2016; Ruhunusiri et al., 2016; Wang & Nielsen, 2003). The upper atmosphere is also influenced by energy and momentum sources from the lower atmosphere via upward propagating atmospheric waves (e.g., Bougher et al., 2004; Bougher, Jakosky, et al., 2015; Fritts et al., 2006; Keating et al., 1998; Medvedev & Yiğit, 2012; Medvedev et al., 2011; Wang & Nielsen, 2004; Withers et al., 2003, 2006; Yiğit et al., 2015). As the ion-neutral collision frequency exceeds the ion cyclotron frequency below an ~160 km altitude over strong crustal field regions and an ~225 km altitude over weak field regions in the Martian ionosphere (Opgenoorth et al., 2010; Riousset et al., 2013), the ionospheric plasma is coupled to the neutral constituents via collisions.

The Mars Advanced Radar for Subsurface and Ionosphere Sounding (MARSIS) instrument on board the Mars Express spacecraft has provided over 12 years of remote and in situ measurements pertinent to the structure and variability of the Martian topside ionosphere (Gurnett et al., 2008; Jordan et al., 2009). MARSIS conducts topside sounding of the Martian ionosphere in the Active Ionospheric Sounding (AIS) mode. In the AIS mode, the transmitter sweeps 160 sounding frequency steps between 0.1 and 5.5 MHz. At each frequency step, a 91.4 μs pulse is transmitted and then return signals at the sounding frequency are recorded in 80 time delay bins with 91.4 μs resolution. The frequency sweep takes 1.26 s and is repeated with 7.54 s cadence. For a horizontally stratified ionosphere, the radio waves emitted at a wide range of angles are reflected in a specular fashion at the altitude where the radio frequency, f, equals the electron plasma frequency, f_{pe}, and only vertically propagating waves return back to the spacecraft as illustrated in Figure 1a. The obtained ionospheric

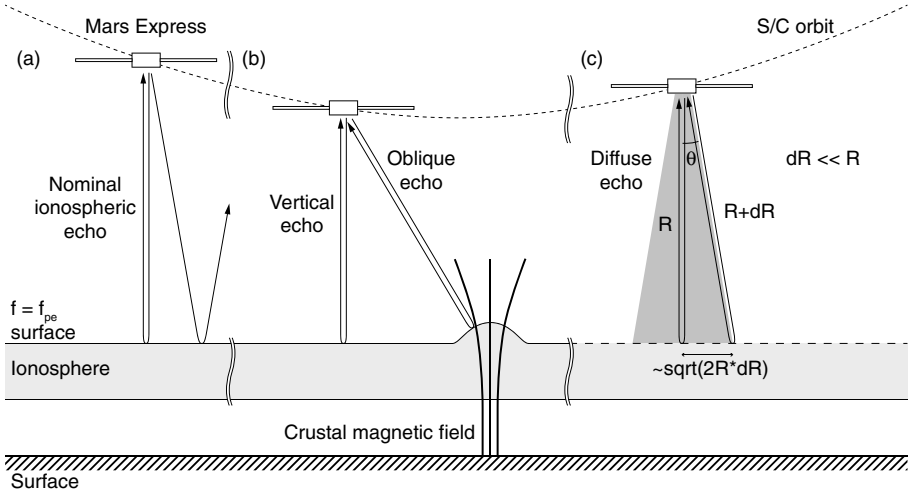

Figure 1. Schematic illustration of MARSIS observation geometry of different types of ionospheric echoes: (a) nominal ionospheric echoes from a horizontally stratified ionosphere, (b) oblique echoes from ionospheric structure above vertical crustal magnetic fields, and (c) diffuse echoes from ionospheric irregularities.

echo trace with the echo time delay as a function of frequency provides information on the vertical electron density profile of the topside ionosphere at altitudes above the maximum electron density.

In addition to remote sensing of electron density profiles (Kopf et al., 2008, 2017; Morgan et al., 2008, 2013) and in situ measurements of local electron density (Andrews et al., 2013; Duru et al., 2008, 2011) and magnetic field strength (Akalin et al., 2010), MARSIS data can be utilized to investigate ionospheric irregularities at Mars because radar sounding is also sensitive to irregular structure in the ionosphere. Ionospheric irregularities have been postulated to cause diffuse nature of ionospheric echoes in MARSIS ionograms (Gurnett et al., 2008), by analogy with spread F ionograms obtained at Earth (e.g., Booker & Wells, 1938). Spread F, one of the oldest topics in the terrestrial aeronomy, represents a collection of phenomena that involve F region irregularities with a wide range of spatial scale sizes observed by a number of different measurement techniques, and its phenomenological properties and physical mechanisms have been extensively studied (Abdu et al., 2012; Booker & Ferguson, 1978; Huang & Kelley, 1996; Kelley et al., 2011; King, 1970; Makela & Otsuka, 2012; Pfaff, 2012; Sales et al., 1996; Tsunoda, 2010a, 2010b; Tsunoda et al., 1982; Woodman, 2009; Wright et al., 1996). However, we note that caution must be exercised when comparing the generation processes of ionospheric irregularities because the topside ionosphere of Mars below ~200 km altitudes is comparable to the terrestrial E region rather than the F region in the sense that ions are unmagnetized while electrons are magnetized as pointed out by Fowler et al. (2017).

Initial in situ measurements by the Mars Atmosphere and Volatile Evolution (MAVEN) mission revealed a high level of interorbit and intraorbit variability of ionospheric and neutral densities (Bougher, Jakosky, et al., 2015), implying the common presence of large density fluctuations in the Martian upper ionosphere. Recently, Fowler et al. (2017) reported MAVEN in situ measurements of electromagnetic irregularities with large density amplitudes up to 200% and spatial scale sizes of 15–20 km in the Martian ionosphere below 200 km altitudes. However, the global distribution, long-term (e.g., seasonal) variability, and generation processes of these ionospheric density fluctuations are yet to be fully elucidated. Characterization of the ionospheric irregularities and identification of their formation mechanisms will help to understand the complex dynamics of the Martian ionosphere driven both by neutral forcing (via atmospheric waves and winds) and by solar forcing (via solar radiation and solar wind). In this paper, we explore the global distribution and variability of ionospheric irregularities that are observed as diffuse echoes by MARSIS topside sounding.

2. Observations

2.1. A Diffuse Echo Event

Figure 2 presents a sample periapsis observation on the dayside. Mars Express traveled over moderately strong crustal magnetic fields in the southern hemisphere during the inbound segment, followed by the outbound segment over the mostly unmagnetized region in the northern hemisphere (Figure 2c). Figure 2a displays a

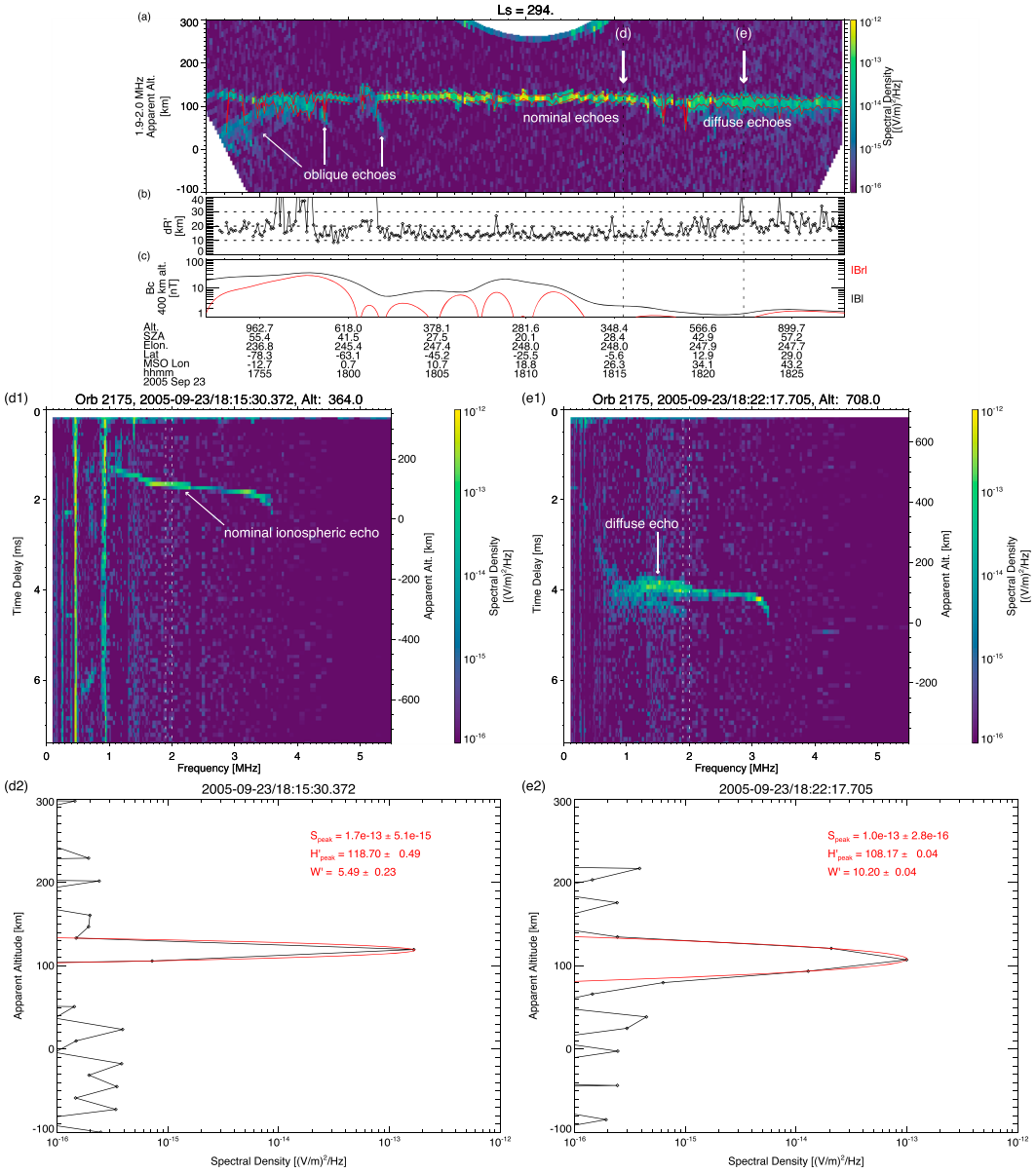

Figure 2. Sample diffuse echo event on 23 September 2005. Time series of (a) echo intensity versus apparent altitude (radargram) for 1.9–2.0 MHz echoes, (b) apparent range spread (dR') derived from Gaussian fitting, and (c) crustal magnetic field strength (black) and magnitude of the radial component (red) at a 400 km altitude at the geographic longitude and latitude of the spacecraft location computed from the spherical harmonic model by Morschhauser et al. (2014). Mars Express altitude, solar zenith angle, geographic east longitude, latitude, and Mars Solar Orbital (MSO) longitude are indicated in the text label. The red lines in Figure 2a represent $H'_{echo} \pm dR'/2$ obtained from the Gaussian fit. Snapshots of the echo intensity at 18:15:30 UT in the ionogram format (d1) and in the H' profile (d2) and at 18:22:17 UT (e1–e2). The vertical dashed lines in Figures 2d1 and 2e1 denote the frequency range of 1.9–2.0 MHz used to produce the radargram (Figure 2a) and H' profiles (Figures 2d2 and 2e2). The red lines in Figures 2d2 and 2e2 show the Gaussian fit results (see text for detail) and the red texts show the best fit parameters with 1-sigma uncertainty estimates obtained in the unknown measurement error approach (Press et al., 1992). The snapshot times are indicated by the arrows and dashed lines in Figures 2a–2c.

radargram of 1.9–2.0 MHz echoes, showing the echo intensity as a function of apparent altitude ($H' = c\Delta t/2$, where c is the speed of light and Δt is the time delay) and time. Note that the apparent altitude, H', is not corrected for plasma dispersion (radio wave propagation slower than c), and H' is lower than the true reflection altitude, H. Primed quantities hereafter refer to apparent distances uncorrected for plasma dispersion, while unprimed counterparts represent true distances. The 1.9–2.0 MHz echoes are reflected from electron densities of $4.5–5.0 \times 10^4$ cm^{-3} typically at H ~160–200 km in the dayside ionosphere (e.g., Ergun et al., 2015; Morgan et al., 2008). We observe a nearly horizontal trace at H' ~120 km (labeled "nominal echoes" in Figure 2a), which represents echoes reflected vertically from a horizontally stratified ionosphere (Figure 1a). Additionally, hyperbola-shaped traces, labeled "oblique echoes" in Figure 2a, are found above the strong crustal magnetic fields (Figure 2c). These oblique echoes are interpreted as ionospheric echoes that return at an oblique angle from a fixed target associated with an upward bulge in the ionosphere on open field lines as illustrated in Figure 1b (Andrews et al., 2014; Diéval et al., 2015; Duru et al., 2006; Gurnett et al., 2005; Nielsen et al., 2007; Venkateswara Rao et al., 2017). The primary ionospheric echo trace at $H' \sim 120$ km is usually narrow with only one or two H' bins (one H' bin corresponding to 13.7 km) showing strong signals. This is expected because the transmitted pulse length (91.4 μs) corresponds to a finite pulse width of 13.7 km in H'. The narrow nature of the nominal ionospheric echo trace is demonstrated in the snapshot at 18:15:30 UT shown in the ionogram format (Figure 2d1, showing the echo intensity as a function of time delay and frequency) and in the H' profile (Figure 2d2). However, the width of the ionospheric echo trace is broadened after 18:19 UT (Figure 2a). As demonstrated in Figures 2e1 and 2e2, significant echo intensity (comparable to the peak intensity) was recorded over three or more H' bins for these diffuse echoes. As these diffuse echoes were observed over very weak crustal magnetic fields (<~2 nT at a 400 km altitude, Figure 2c) and they were not accompanied by hyperbola-shaped traces, we would not classify them as the classical oblique echoes associated with ionospheric structure in strong crustal magnetic fields. It has been proposed that such diffuse echoes are caused by a spread in time delays of a number of off-vertical echoes reflected/scattered from ionospheric irregularities as illustrated in Figure 1c (Gurnett et al., 2008; Harada et al., 2017), detailed properties of which remain unclear.

To quantify the diffuseness of ionospheric echoes, we conduct least squares fitting to the measured H' profiles of the echo intensity by a Gaussian profile,

$$S(H') = S_{\mathrm{peak}} \exp\left(\frac{-(H' - H'_{\mathrm{peak}})^2}{W'^2}\right), \tag{1}$$

where $S(H')$ is the echo spectral density as a function of apparent altitude, S_{peak} is the peak intensity, H'_{peak} is the apparent altitude of the peak center, and W' is the e-folding half width. To represent the width of the return pulse, we take a full width of 1/2 peak amplitude (1/4 peak power) and define an apparent range spread as $\mathrm{d}R' \equiv (2\sqrt{2\ln 2})W'$, which can be derived from $1/4 = \exp(-(\mathrm{d}R'/2)^2/W'^2)$ (note that the transmitted pulses reach 1/2 amplitude immediately after the impulse commences; see Figure 6 of Morgan et al., 2013). We fit the Gaussian profile to the measured echo intensity profile in a range between 20 km < H' < 200 km, thereby obtaining best fit values of the Gaussian parameters, S_{peak}, H'_{peak}, and W'. The red lines in Figures 2d2 and 2e2 display fitting results for the sample echo profiles. We note that as we conduct least squares fitting in a *linear* scale, our fitting procedure preferentially evaluates data points with echo intensities comparable to the peak intensity. Therefore, $\mathrm{d}R'$ represents the width of the primary peak and does not capture weak signals at high- and low-altitude tails of the peak.

We repeat the Gaussian fitting procedure for each time step. To ensure clean profiles of ionospheric echoes, we reject H' profiles if the maximum intensity is less than 10^{-15} (V/m)^2/Hz (thereby excluding profiles with extremely weak echoes or no echoes). We also require that at least one data point above the maximum intensity altitude is at least an order of magnitude smaller than the maximum intensity, and similarly below the maximum intensity altitude (thereby filtering out "flat" profiles which happen when plasma oscillation harmonics contaminate the echo profile). Figure 2b shows a time series of the best fit $\mathrm{d}R'$, while the red lines in Figure 2a represent $H'_{\mathrm{peak}} \pm \mathrm{d}R'/2$. We observe small $\mathrm{d}R'$ (~13 km) for the nominal echoes and consistently large $\mathrm{d}R'$ (~20 km) for diffuse echoes, demonstrating that our fitting procedure successfully captures the diffuseness of primary ionospheric echoes. It is also seen in the inbound segment that large $\mathrm{d}R'$ can be caused by overlapped multiple traces in the presence of the oblique echoes above strong crustal magnetic fields.

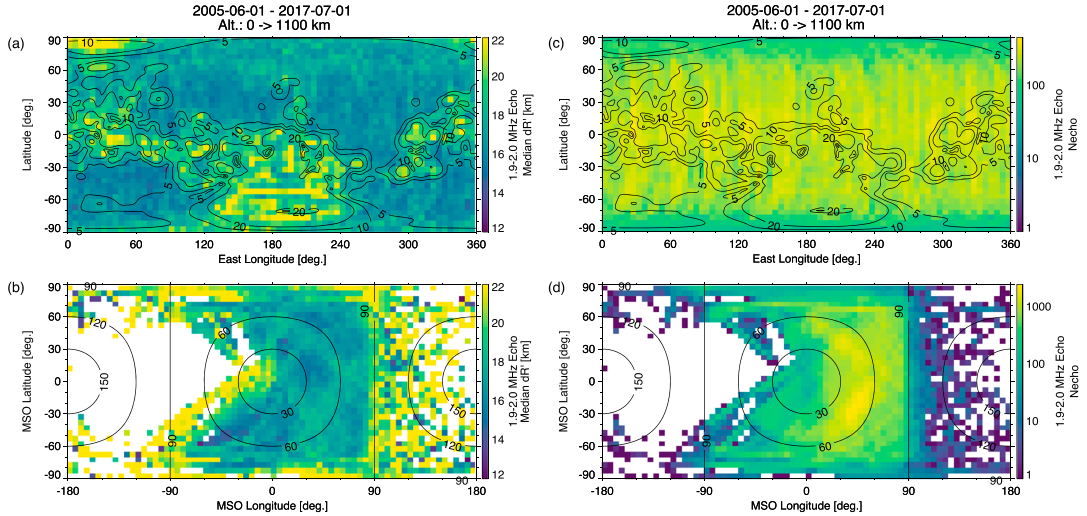

Figure 3. Median apparent range spread (dR') of ionospheric echoes in (a) geographic and (b) MSO coordinates. Number of echoes in (c) geographic and (d) MSO coordinates used to generate Figures 3a and 3d. The black contours in Figures 3a and 3c show the crustal magnetic field strength, $|B_c|$, at a 400 km altitude. The black contours in Figures 3b and 3d denote solar zenith angles.

2.2. Data Processing

In this paper, we present analysis of 1.9–2.0 MHz echoes. We chose this frequency range based on two competing factors: (i) mitigating contamination from plasma oscillation harmonics and electron cyclotron echoes (higher frequencies are better because the contamination is more significant at lower frequencies) and (ii) obtaining a larger number of ionospheric echoes (lower frequencies are better because ionospheric echoes are detectable over a wider range of solar zenith angles). We note that we performed the same procedure for other frequency ranges between 1.5 MHz and 2.6 MHz and obtained qualitatively similar results.

We utilize a long-term MARSIS data set obtained from June 2005 to June 2017 at spacecraft altitudes lower than 1,100 km (thereby ensuring that ionospheric echoes can be detected within the measured time delay range). We perform the Gaussian fitting to each of the measured H' profiles of echo intensities that satisfy the selection criteria described in section 2.1. Figures 3a and 3b show geographic and Mars Solar Orbital (MSO) distributions of median values of the best fit dR' in $5° \times 5°$ bins. The MSO coordinate system is defined in such a way that the x axis points from Mars toward the Sun, y points opposite to the direction of Mars' orbital velocity component perpendicular to x, and z completes the orthogonal coordinate set. Negative (positive) MSO longitudes correspond to the dawnside (duskside) of Mars. This ionospheric echo data set provides nearly uniform geographic coverage (Figures 3c), but the MSO sampling is highly nonuniform (Figure 3d) owing to the biased orbital coverage (the dawnside is not well sampled) and the lack of usable profiles on the nightside (where detectable ionospheric echoes are typically absent at 1.9–2.0 MHz (Diéval et al., 2014; Němec et al., 2010, 2011)). The observed apparent range spread shows a clear correlation with the crustal magnetic field strength (Figure 3a) as expected from the enhanced dR' caused by overlapping of the vertical and oblique echo traces above strong crustal magnetic fields (Figures 2a-2c). As our main interest here is the diffuse echoes detected above unmagnetized regions, we exclude data obtained above magnetized regions with $|B_c| > 5$ nT at a 400 km altitude in the following analysis, resulting in removal of about a half of the echo data.

2.3. Properties of Diffuse Echoes

2.3.1. Range Dependence

We first investigate dR' dependence on the observation geometry, specifically on spacecraft altitudes, $H_{S/C}$. As the state of the ionosphere is not influenced by spacecraft altitudes, any dependence of dR' on $H_{S/C}$ is nongeophysical and must be corrected before combining data obtained at different spacecraft altitudes. Figure 4 shows the apparent range spread (dR') as a function of apparent range of the vertical echo ($R' \equiv H_{S/C} - H'_{peak} - dR'/2$, which represents the apparent distance to the upper edge of the echo profile). Since the spacecraft altitude varies more widely compared with the ionospheric height, most of the echo range variations originate from the variation in spacecraft altitudes. We observe a clear linear relation with a nonzero offset as demonstrated by the linear fit shown in red in Figure 4. The nonzero offset, $dR'_0 = 13.2$ km, can be explained by the finite length of the transmitted pulse (91.4 μs, corresponding to the apparent range

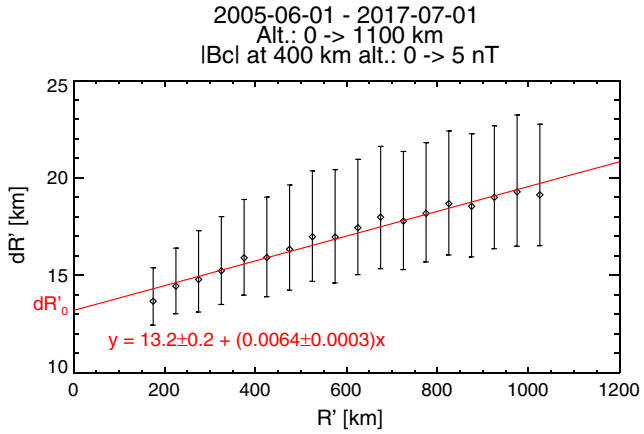

Figure 4. Apparent range spread (dR') versus apparent range (R') plot from ionospheric echoes detected above unmagnetized regions. The black diamonds with error bars represent the median dR' with quartiles in 50 km R' bins. The red line shows linear fitting to the medians, and the equation in red shows the best fit parameters with 1-sigma uncertainty estimates.

width of 13.7 km). If we define an excess apparent range, $dR'_{ex} \equiv dR' - dR'_0$, then dR'_{ex} is proportional to R'. Given that the excess time delay is proportional to the additional echo path length compared with the shortest (vertical) return path, the proportional relation between dR'_{ex} and R' indicates that the angle of arrival, $\theta \sim \arctan(\sqrt{2dR/R})$, where R is the vertical echo range and dR is the excess range (Figure 1c), is independent of spacecraft altitudes. This suggests that the extent of the measured range spread is determined by the angular extent of return echoes, not by the horizontal extent of the reflection/scattering target ($\sim 2\sqrt{2RdR}$, see Figure 1c) nor by altitude variations of reflection sources within the first Fresnel zone (in which case dR should be independent of R). Assuming that the ratio of apparent lengthening by dispersion is similar for vertical and oblique paths ($R'/R \sim (R' + dR'_{ex})/(R + dR)$ and therefore $dR/R \sim dR'_{ex}/R'$), we approximate the angular extent of return echoes by $\theta \sim \arctan(\sqrt{2dR'_{ex}/R'})$.

The echo angular extent, θ, represents a measure of echo diffuseness corrected for the range dependence, providing information on ionospheric irregularities that are responsible for producing the diffuse nature of ionospheric echoes. Figure 5 shows geographic and MSO distributions of the echo angular extent and data density for unmagnetized regions. The median of the echo angular extent detected above unmagnetized regions is 6.4° , and the lower and upper quartiles are 3.7° and 9.0° , respectively. On average, we do not find any prominent dependence on geographic location (Figure 5a), whereas we observe larger angular extents near the terminator and on the nightside (Figure 5b). This solar zenith angle dependence is directly demonstrated in Figure 6, which clearly shows the elevated level of echo angular extent at high solar zenith angles.

2.3.2. Seasonal Variability

We now investigate seasonal variability of ionospheric irregularities. As the state of the upper atmosphere varies dramatically with season (e.g., Bougher, Pawlowski, et al., 2015), conditions for the ionospheric irregularity generation might change with season. Figure 7 shows geographic and MSO distributions of the echo angular extent separated for four different solar longitude (L_S) ranges. Both the geographic and MSO distributions exhibit remarkable north-south asymmetry during the solstices (Figures 7c, 7d, 7g, and 7h). The median angular extent is significantly enhanced in the winter hemisphere, namely, in the southern hemisphere during the northern summer solstice (Figures 7c and 7d) and in the northern hemisphere during the northern winter

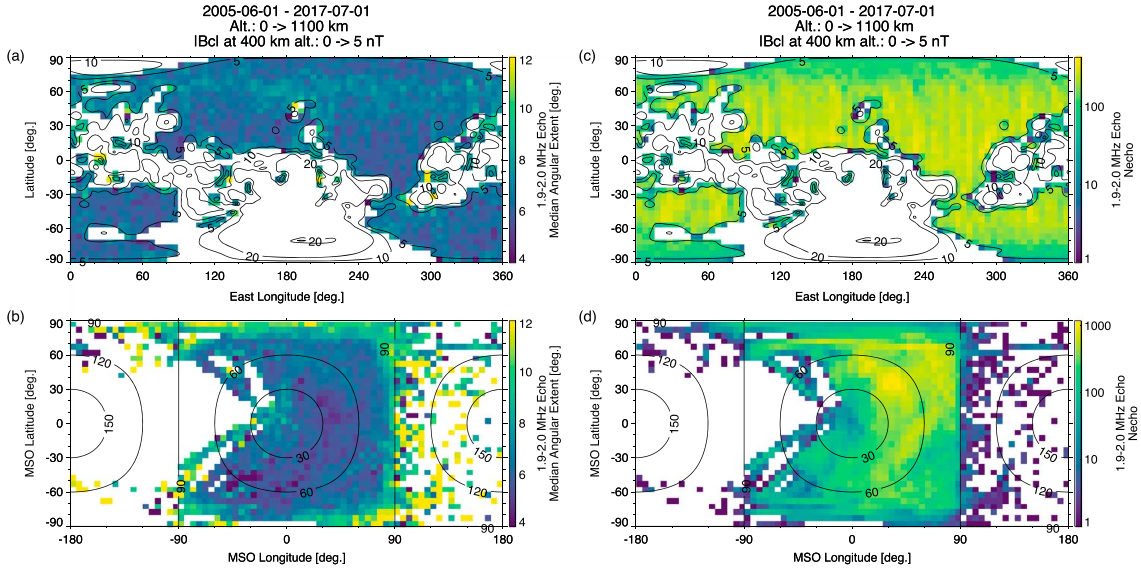

Figure 5. Median angular extents of ionospheric echoes above unmagnetized regions in (a) geographic and (b) MSO coordinates. Number of echoes in (c) geographic and (d) MSO coordinates used to generate Figures 5a and 5d.

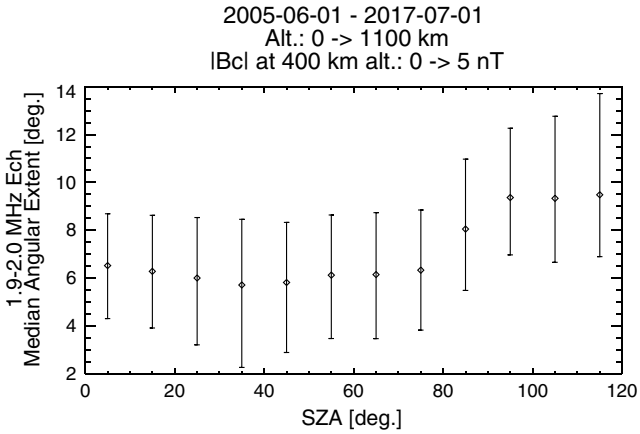

Figure 6. Echo angular extent versus solar zenith angle (SZA) plot from ionospheric echoes detected above unmagnetized regions. The diamonds with error bars represent the median values with quartiles in 10° SZA bins.

solstice (Figures 7g and 7h). Meanwhile, the equinox data show intermediate states between the solstices with no obvious north-south asymmetry (Figures 7a, 7b, 7e, and 7f). We do not see any clear dependence on geographic longitudes (Figures 7a, 7c, 7e, and 7g). Figure 8 shows echo angular extent versus L_S plots for the northern and southern hemispheres. It is clearly seen that the angular extent distribution shifts systematically toward larger values in the winter hemisphere ($L_S \sim 270°$ in Figure 8a and $L_S \sim 90°$ in Figure 8b) compared with the summer hemisphere ($L_S \sim 90°$ in Figure 8a and $L_S \sim 270°$ in Figure 8b). The prominent enhancement of the echo angular extent in the winter hemisphere suggests that some kind of atmospheric and/or ionospheric conditions in the winter hemisphere are favorable for generation of ionospheric irregularities.

We briefly discuss dependence of ionospheric irregularities on the Mars-Sun distance, which varies with season. We first point out that the observed north-south asymmetry must reflect seasonal dependence because the Mars-Sun distance does not differ in the northern and southern hemispheres in a particular season. Meanwhile, the slightly higher median peak at ~7.9° around $L_S \sim 270°$ (close to the perihelion) in Figure 8a compared to the peak at ~7.4° around $L_S \sim 90°$ (close to the aphelion) in Figure 8b might be caused by the different Mars-Sun distances. However, this shift is much smaller than the seasonal variation.

2.3.3. Solar Wind Control

Next we examine dependence of the echo angular extent on the solar wind condition. To organize the MARSIS data according to the solar wind condition, we utilize solar wind ion parameters measured by the Solar Wind Ion Analyzer (SWIA) on board MAVEN (Halekas, Ruhunusiri, et al., 2016) as well as the subsolar magnetic field strength derived from Mars Global Surveyor (MGS) measurements as a proxy for the upstream pressure (Brain et al., 2005). Simultaneous measurements of the upstream pressure and ionospheric sounding are available for limited intervals (after October 2014 for SWIA-MARSIS and until November 2006 for MGS-MARSIS), resulting in substantial reduction in the data volume. In Figure 9, we present histograms of the echo angular extent for high and low solar wind dynamic pressure conditions during each season. During the northern summer solstice for the SWIA interval and the equinoxes for the MGS interval, only very small numbers of echoes are available (<3,000) and we do not find any meaningful trends in these statistically poor histograms (not shown). A common feature among the shown histograms is that the major parts near the peaks of event distributions remain unchanged for varying solar wind conditions. In Figures 9a, 9b, and 9d, extreme events (e.g., $\theta > 15°$) in the minor tail distributions are observed more frequently for the high dynamic pressures compared to the low pressures, but this trend is less clear in Figure 9e and no difference is seen in Figure 9c. The inconsistent response to variations in solar wind dynamic pressures during different time intervals implies that the solar wind may modify the nature of diffuse echoes in a complex manner, details of which remain elusive.

3. Discussion

3.1. Scale Size of Ionospheric Irregularities

We first discuss the spatial scale size of ionospheric irregularities that cause the diffuse echoes detected by MARSIS. Depending on the irregularity scale size, several reflection/scattering processes can give rise to diffuse nature of ionospheric echoes as extensively studied for spread F ionograms at Earth (e.g., Wright et al., 1996). If the scale size of the irregularity, λ_{irr}, is larger than the first Fresnel zone diameter, L_F, the transmitted radio waves reflect in a specular manner from ionization surfaces (this process is called total reflection as opposed to scattering discussed later). In this case, diffuse traces in ionograms result from unresolved traces of multiple off-vertical echoes reflected from undulated iso-density surfaces (Bowman, 1990; King, 1970; Reinisch et al., 2004; Tsunoda, 2010a). Diffuse traces can be also caused by scattering from small-scale irregularities with $\lambda_{irr} < L_F$. In particular, possible explanations for spread F ionograms have been discussed in terms of scattering from irregularities with $\lambda_{irr} \sim \lambda/2$, where λ is the radio wavelength, (coherent/Bragg scatter) (Abdu et al., 2012; Booker & Ferguson, 1978; Sales et al., 1996) and from those with $\lambda_{irr} \ll \lambda$ (Rayleigh scatter) (Booker & Wells, 1938). For MARSIS observations of 1.9–2.0 MHz echoes, the radio wavelength is $\lambda \sim 150$ m, the echo range is $R \sim 200$–1,000 km, and the Fresnel scale is $L_F \sim 10$–20 km.

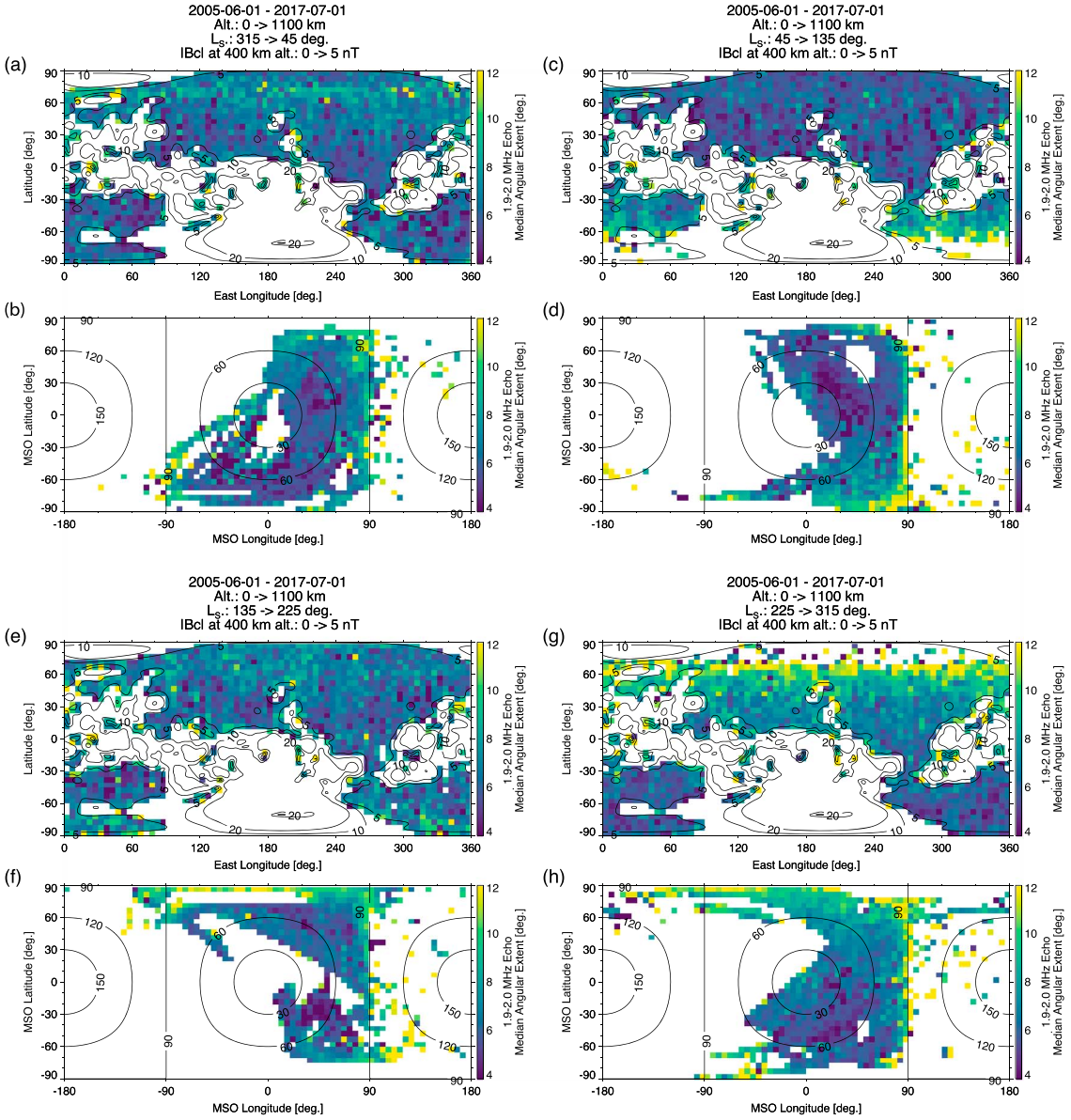

Figure 7. Median angular extents of ionospheric echoes above unmagnetized regions in (a) geographic and (b) MSO coordinates during the northern spring equinox ($L_S \sim 0°$), (c, d) summer solstice ($L_S \sim 90°$), (e, f) autumn equinox ($L_S \sim 180°$), and (g, h) winter solstice ($L_S \sim 270°$).

We now compare the observed echo properties with the expected ones for different size irregularities. We consider how the reflection and scattering processes alter the nature of ionospheric echoes measured by MARSIS for three ranges of irregularity scale sizes: (i) $\lambda_{irr} > R$, (ii) $L_F < \lambda_{irr} < R$, and (iii) $\lambda_{irr} < L_F$ as illustrated in Figure 10.

First, if the irregularity size is larger than the echo range ($\lambda_{irr} > R$), MARSIS will detect a single echo reflected from a tilted iso-density surface (Figure 10a), which will not lead to diffuse echoes. Therefore, planetary-scale ionospheric structure with $\lambda_{irr} > 1,000$ km cannot explain the diffuse nature of ionospheric echoes.

Second, total reflection from a wavy surface with $L_F < \lambda_{irr} < R$ will produce multiple specularly reflected echoes (Figure 10b), which may be detected as unresolved diffuse traces given the relatively coarse time delay resolution of MARSIS. As illustrated in Figure 10b, the angular extent of specularly reflected echoes is geometrically restricted by the maximum inclination of the reflection surface. Assuming a sinusoidal undulation of $dH \sin(2\pi x/\lambda_{irr})$, where dH is the amplitude of the reflection surface undulation and x is the horizontal distance, the maximum inclination is derived as $2\pi dH/\lambda_{irr}$. In this model, the echo angular extent is determined

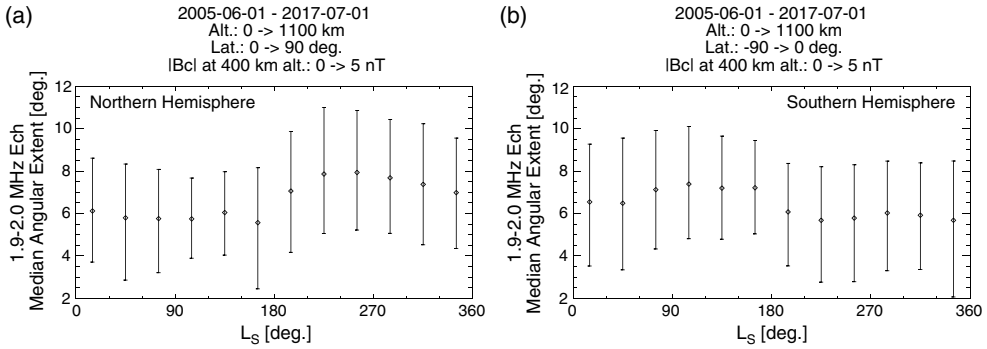

Figure 8. Echo angular extent versus solar longitude (L_S) plot from ionospheric echoes detected above unmagnetized regions in the geographic (a) northern and (b) southern hemispheres. The diamonds with error bars represent the median values with quartiles in 30° L_S bins.

by the ratio between the amplitude and wavelength of relevant irregularities, which can explain the observed independence of echo angular extents from spacecraft altitudes. Using a typical value of $\theta \sim 8°$ of the observed diffuse echoes in the winter hemisphere (e.g., Figures 7 and 8), we obtain $dH/\lambda_{irr} \sim 0.02$. Based on these observations, the properties of diffuse echoes detected by MARSIS are consistent with total reflection from ionospheric irregularities with tens of kilometers $< \lambda_{irr} <$ hundreds of kilometers and vertical undulation amplitudes of a few percent of the horizontal scale sizes.

Finally, scattering from small-scale irregularities with $\lambda_{irr} < L_F$ can cause range spread as additional paths can be obtained by backscatter at oblique incidence and/or multiple scattering (Figure 10c). However, intensities of these scattered echoes are estimated to be at least 2 orders of magnitude weaker than those of total reflection echoes (Bowman, 1990; King, 1970; Wright et al., 1996). The expected weak signals are inconsistent with the diffuse echoes analyzed in this paper because our fitting procedure only concerns relatively strong echoes with intensities comparable to the primary peak. Furthermore, these scattering processes do not necessarily require echo angular extents to be independent of echo ranges. Thus, it is unlikely that scattering from subkilometer scale irregularities is the dominant process that causes the relatively strong diffuse echoes measured by MARSIS.

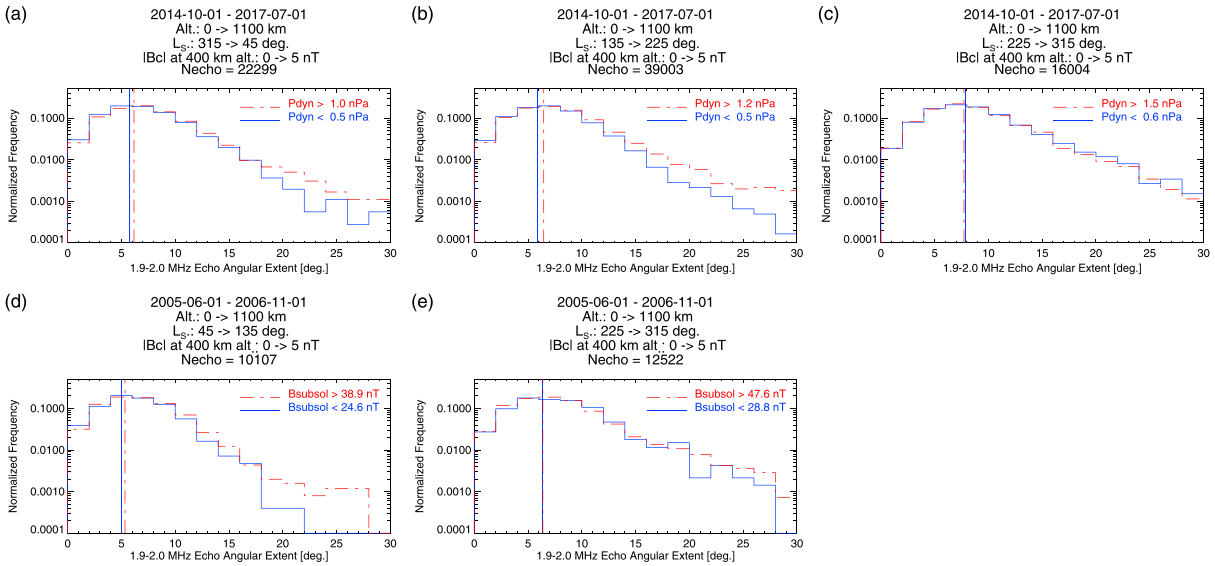

Figure 9. Normalized histograms of angular extents of ionospheric echoes above unmagnetized regions for high solar wind dynamic pressure conditions (dot-dashed red lines, higher than the upper quartile) and low dynamic pressure conditions (solid blue lines, lower than the lower quartile) during (a) the northern spring equinox ($L_S \sim 0°$), (b) autumn equinox ($L_S \sim 180°$), and (c) winter solstice ($L_S \sim 270°$) according to the MAVEN SWIA data, and those during (d) the northern summer solstice ($L_S \sim 90°$), and (e) winter solstice ($L_S \sim 270°$) based on the MGS upstream pressure proxy data. The vertical lines denote the median value for each condition.

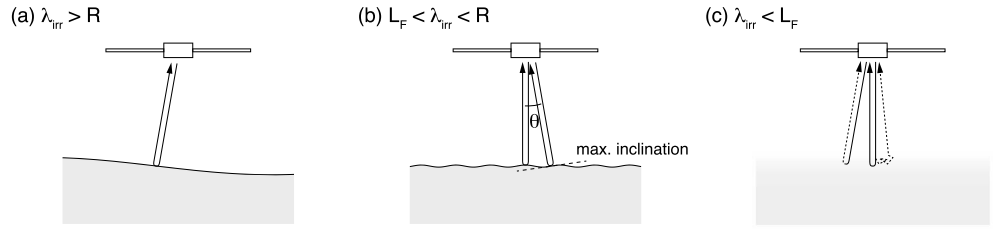

Figure 10. Schematics illustrating that ionospheric irregularities modify echo properties in a variety of ways depending on the horizontal scale size of irregularities (λ_{irr}) with respect to the echo range (R) and the first Fresnel zone diameter (L_F).

Having explored a wide range of irregularity scale sizes, we conclude that total (specular) reflection from ionospheric irregularities with horizontal scale sizes of tens to hundreds of kilometers is the most likely explanation for the diffuse echoes measured by MARSIS.

3.2. Driving Processes

We now explore geophysical processes that generate the ionospheric irregularities at ~160–200 km altitudes probed by MARSIS. The diffuse echo observations exhibit systematic preferences for high solar zenith angles and the winter hemisphere (Figures 5–8). One possible explanation for this trend is provided by internal gravity waves (GWs) in the Martian neutral thermosphere. MAVEN observations revealed that density amplitudes of GWs with horizontal wavelengths of ~100–500 km around the exobase (~180–220 km altitudes) are on the order of ~10–20% on average and are anticorrelated with the background atmospheric temperature (England et al., 2017; Terada et al., 2017). The background atmospheric temperature around the exobase decreases at high solar zenith angles and in the winter hemisphere (e.g., Bougher, Pawlowski, et al., 2015). Figure 11 shows MARSIS echo angular extents organized by predicted neutral atmospheric temperatures from the Mars Global Ionosphere-Thermosphere Model (M-GITM) (Bougher, Pawlowski, et al., 2015; Bougher, Cravens, et al., 2015). We observe clear inverse dependence of echo angular extents on the predicted neutral temperature, suggesting that large-amplitude ionospheric irregularities coincide with large-amplitude neutral GWs. The lack of geographic dependence is another common feature in the observations of neutral GWs (Terada et al., 2017) and ionospheric irregularities (Figures 5 and 7). In situ measurements of thermal ions and neutrals by MAVEN demonstrate the presence of ion density oscillations closely associated with neutral GWs (Bougher, Jakosky, et al., 2015; Grebowsky et al., 2017). Note that the horizontal wavelengths of the observed GWs are also consistent with those estimated for the ionospheric irregularities probed by MARSIS (tens to hundreds of kilometers, see section 3.1). The observed correlation between neutral GW amplitudes and ionospheric irregularities implies that neutral GWs in the Martian thermosphere provide a dominant driver for plasma perturbations around the exobase.

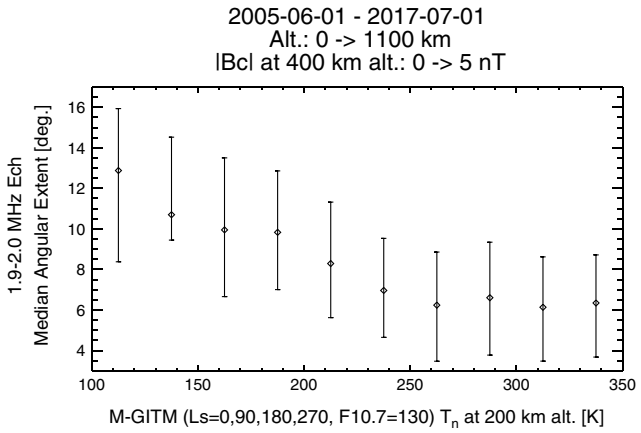

Figure 11. Echo angular extent versus predicted neutral temperature (T_n) plot from ionospheric echoes detected above unmagnetized regions, with T_n from the M-GITM model (Bougher, Pawlowski, et al., 2015; Bougher, Cravens, et al., 2015). The diamonds with error bars represent the median values with quartiles in 25 K T_n bins. T_n for a given MARSIS measurement is taken from the corresponding (local time, latitude) bin at a 200 km altitude in areodetic vertical coordinates of three-dimentional data cubes for the moderate solar activity M-GITM simulation during each season (L_S = 0°, 90°, 180°, and 270°), available at https://lasp.colorado.edu/maven/sdc/public/pages/models.html.

We observe limited influence of varying solar wind conditions on diffuse echoes (Figure 9). The major parts of the angular extent distributions remain unchanged for high and low dynamic pressure conditions. The minor tail distributions consisting of extreme events are enhanced for high solar wind dynamic pressures during some intervals, but they do not change during other intervals. Though the reasons for this inconsistent behavior of extreme events remain unclear, it appears that ionospheric perturbations by the solar wind energy input alone cannot account for the majority of ionospheric irregularities probed by MARSIS. In comparison with the clear seasonal dependence shown in Figures 7 and 8, the solar wind driver seems to have less significant effects on the production of ionospheric irregularities. We note that neutral GW observations also show no clear dependence on solar wind parameters (Terada et al., 2017).

Here we briefly discuss the role of plasma instabilities in the generation of ionospheric irregularities at Mars. For the nighttime equatorial spread F at Earth, the formation of plasma bubbles and associated ionospheric

irregularities is generally explained by the combination of the gravity-driven Rayleigh-Taylor instability and seeding from GWs and/or shear flows (Kelley et al., 2011; Makela & Otsuka, 2012; Pfaff, 2012; Tsunoda, 2010a, 2010b; Woodman, 2009). Though basic phenomenological properties of the equatorial plasma bubbles are consistent with the Rayleigh-Taylor instability, the seeding mechanisms are needed to overcome the slow growth rate of the instability and explain the significant day-to-day variability in the spread F occurrence. At Mars, the observed seasonal dependence of diffuse echoes in the MARSIS data indicates a direct correlation between ionospheric irregularities and atmospheric GWs, suggesting that GWs play a central role in controlling the occurrence of the ionospheric irregularities. This implies that plasma instabilities may uniformly contribute to the growth of GW-driven plasma perturbations or that they do not play any significant role in generating the ionospheric irregularities.

4. Conclusions

We present MARSIS observations of diffuse ionospheric echoes, which are indicative of ionospheric irregularities deviated from a horizontally stratified ionosphere. We analyzed a long-term MARSIS data set obtained above unmagnetized regions and identified a linear relation between the echo range (mainly determined by the spacecraft altitude) and range spread, suggesting that the echo angular extent represents the state of perturbed reflection surfaces. The observed properties of diffuse echoes are consistent with total/specular reflection from undulated iso-density surfaces with horizontal wavelengths of tens to hundreds of kilometers and vertical amplitudes of a few percent of the horizontal wavelengths. The echo angular extent increases significantly at high solar zenith angles and in the winter hemisphere, where lower atmospheric temperatures are expected. Having explored possible drivers of ionospheric irregularities (neutral GWs, solar wind forcing, and plasma instabilities), we conclude that the majority of the observed ionospheric irregularities are driven by neutral GWs in the Martian thermosphere for the following reasons: (i) known association of ion density variations (i.e., ionospheric irregularities) with neutral gravity waves at Mars, (ii) comparable horizontal wavelengths, (iii) large-amplitude gravity waves and large-amplitude ionospheric irregularities observed in similar latitudes/seasons (i.e., cold locations), and (iv) broad geographic distributions of gravity waves and ionospheric irregularities. The solar wind forcing seems to play a limited role in generation of these ionospheric irregularities. The global and long-term remote measurements of ionospheric irregularities by MARSIS can be combined with in situ measurements by MAVEN in a complementary fashion for an improved understanding of dynamics of the ionosphere and its coupling to the neutral atmosphere at Mars.

Acknowledgments
The MARSIS investigation at the University of Iowa was supported by NASA through contract 1560641 with the Jet Propulsion Laboratory. MARSIS data are available through the Planetary Data System at http://pds-geosciences.wustl.edu. MAVEN data are publicly available through the Planetary Data System at https://pds-ppi.igpp.ucla.edu. The authors gratefully acknowledge D. A. Brain for providing the MGS proxy data through his website at http://sprg.ssl.berkeley.edu/~brain/proxies/subsolfield. The authors acknowledge S. W. Bougher for providing the M-GITM simulation results through the public MAVEN SDC website at https://lasp.colorado.edu/maven/sdc/public/pages/models.html.

References

Abdu, M. A., Batista, I. S., Reinisch, B. W., MacDougall, J. W., Kherani, E. A., & Sobral, J. H. A. (2012). Equatorial range spread F echoes from coherent backscatter, and irregularity growth processes, from conjugate point digital ionograms. *Radio Science*, *47*, RS6003. https://doi.org/10.1029/2012RS005002

Akalin, F., Morgan, D., Gurnett, D., Kirchner, D., Brain, D., Modolo, R., … Espley, J. (2010). Dayside induced magnetic field in the ionosphere of Mars. *Icarus*, *206*(1), 104–111. https://doi.org/10.1016/j.icarus.2009.03.021

Andrews, D. J., André, M., Opgenoorth, H. J., Edberg, N. J. T., Diéval, C., Duru, F., … Witasse, O. (2014). Oblique reflections in the Mars Express MARSIS data set: Stable density structures in the Martian ionosphere. *Journal of Geophysical Research: Space Physics*, *119*, 3944–3960. https://doi.org/10.1002/2013JA019697

Andrews, D. J., Opgenoorth, H. J., Edberg, N. J. T., André, M., Fränz, M., Dubinin, E., … Witasse, O. (2013). Determination of local plasma densities with the MARSIS radar: Asymmetries in the high-altitude Martian ionosphere. *Journal of Geophysical Research: Space Physics*, *118*, 6228–6242. https://doi.org/10.1002/jgra.50593

Booker, H. G., & Ferguson, J. A. (1978). A theoretical model for equatorial ionospheric spread-F echoes in the HF and VHF bands. *Journal of Atmospheric and Solar-Terrestrial Physics*, *40*(7), 803–829. https://doi.org/10.1016/0021-9169(78)90032-6

Booker, H. G., & Wells, H. W. (1938). Scattering of radio waves by the *F*-region of the ionosphere. *Terrestrial Magnetism and Atmospheric Electricity*, *43*(3), 249–256. https://doi.org/10.1029/TE043i003p00249

Bougher, S. W., Cravens, T. E., Grebowsky, J., & Luhmann, J. (2015). The aeronomy of Mars: Characterization by MAVEN of the upper atmosphere reservoir that regulates volatile escape. *Space Science Reviews*, *195*(1), 423–456. https://doi.org/10.1007/s11214-014-0053-7

Bougher, S. W., Engel, S., Hinson, D. P., & Murphy, J. R. (2004). MGS Radio Science electron density profiles: Interannual variability and implications for the Martian neutral atmosphere. *Journal of Geophysical Research*, *109*, E03010. https://doi.org/10.1029/2003JE002154

Bougher, S., Jakosky, B., Halekas, J., Grebowsky, J., Luhmann, J., Mahaffy, P., … Yelle, R. (2015). Early MAVEN deep dip campaign reveals thermosphere and ionosphere variability. *Science*, *350*(6261), 0459. https://doi.org/10.1126/science.aad0459

Bougher, S. W., Pawlowski, D., Bell, J. M., Nelli, S., McDunn, T., Murphy, J. R., … Ridley, A. (2015). Mars global ionosphere-thermosphere model: Solar cycle, seasonal, and diurnal variations of the Mars upper atmosphere. *Journal of Geophysical Research: Planets*, *120*, 311–342. https://doi.org/10.1002/2014JE004715

Bowman, G. G. (1990). A review of some recent work on mid-latitude spread-f occurrence as detected by ionosondes. *Journal of Geomagnetism and Geoelectricity*, *42*(2), 109–138. https://doi.org/10.5636/jgg.42.109

Brain, D. A., Halekas, J. S., Lillis, R., Mitchell, D. L., Lin, R. P., & Crider, D. H. (2005). Variability of the altitude of the Martian sheath. *Geophysical Research Letters*, *32*, L18203. https://doi.org/10.1029/2005GL023126

Diéval, C., Andrews, D. J., Morgan, D. D., Brain, D. A., & Gurnett, D. A. (2015). MARSIS remote sounding of localized density structures in the dayside Martian ionosphere: A study of controlling parameters. *Journal of Geophysical Research: Space Physics*, *120*, 8125–8145. https://doi.org/10.1002/2015JA021486

Diéval, C., Morgan, D. D., Němec, F., & Gurnett, D. A. (2014). MARSIS observations of the Martian nightside ionosphere dependence on solar wind conditions. *Journal of Geophysical Research: Space Physics*, *119*, 4077–4093. https://doi.org/10.1002/2014JA019788

Dubinin, E., Fraenz, M., Woch, J., Duru, F., Gurnett, D., Modolo, R., … Lundin, R. (2009). Ionospheric storms on Mars: Impact of the corotating interaction region. *Geophysical Research Letters*, *36*, L01105. https://doi.org/10.1029/2008GL036559

Dubinin, E., Modolo, R., Fraenz, M., Woch, J., Duru, F., Akalin, F., … Picardi, G. (2008). Structure and dynamics of the solar wind/ionosphere interface on Mars: MEX-ASPERA-3 and MEX-MARSIS observations. *Geophysical Research Letters*, *35*, L11103. https://doi.org/10.1029/2008GL033730

Duru, F., Gurnett, D. A., Averkamp, T. F., Kirchner, D. L., Huff, R. L., Persoon, A. M., … Picardi, G. (2006). Magnetically controlled structures in the ionosphere of Mars. *Journal of Geophysical Research*, *111*, A12204. https://doi.org/10.1029/2006JA011975

Duru, F., Gurnett, D. A., Morgan, D. D., Modolo, R., Nagy, A. F., & Najib, D. (2008). Electron densities in the upper ionosphere of Mars from the excitation of electron plasma oscillations. *Journal of Geophysical Research*, *113*, A07302. https://doi.org/10.1029/2008JA013073

Duru, F., Gurnett, D. A., Morgan, D. D., Winningham, J. D., Frahm, R. A., & Nagy, A. F. (2011). Nightside ionosphere of Mars studied with local electron densities: A general overview and electron density depressions. *Journal of Geophysical Research*, *116*, A10316. https://doi.org/10.1029/2011JA016835

England, S. L., Liu, G., Yiğit, E., Mahaffy, P. R., Elrod, M., Benna, M., … Jakosky, B. (2017). MAVEN NGIMS observations of atmospheric gravity waves in the Martian thermosphere. *Journal of Geophysical Research: Space Physics*, *122*, 2310–2335. https://doi.org/10.1002/2016JA023475

Ergun, R. E., Morooka, M. W., Andersson, L. A., Fowler, C. M., Delory, G. T., Andrews, D. J., … Jakosky, B. M. (2015). Dayside electron temperature and density profiles at Mars: First results from the MAVEN Langmuir probe and waves instrument. *Geophysical Research Letters*, *42*, 8846–8853. https://doi.org/10.1002/2015GL065280

Fowler, C. M., Andersson, L., Shaver, S. R., Thayer, J. P., Huba, J. D., Lillis, R., … Jakosky, B. M. (2017). MAVEN Observations of Ionospheric Irregularities at Mars. *Geophysical Research Letters*, *44*, 10,845–10,854. https://doi.org/10.1002/2017GL075189

Fritts, D. C., Wang, L., & Tolson, R. H. (2006). Mean and gravity wave structures and variability in the Mars upper atmosphere inferred from Mars Global Surveyor and Mars Odyssey aerobraking densities. *Journal of Geophysical Research*, *111*, A12304. https://doi.org/10.1029/2006JA011897

Grebowsky, J. M., Benna, M., Plane, J. M. C., Collinson, G. A., Mahaffy, P. R., & Jakosky, B. M. (2017). Unique, non-Earthlike, meteoritic ion behavior in upper atmosphere of Mars. *Geophysical Research Letters*, *44*, 3066–3072. https://doi.org/10.1002/2017GL072635

Gurnett, D., Huff, R., Morgan, D., Persoon, A., Averkamp, T., Kirchner, D., … Picardi, G. (2008). An overview of radar soundings of the Martian ionosphere from the Mars Express spacecraft. *Advances in Space Research*, *41*(9), 1335–1346. https://doi.org/10.1016/j.asr.2007.01.062

Gurnett, D. A., Kirchner, D. L., Huff, R. L., Morgan, D. D., Persoon, A. M., Averkamp, T. F., … Picardi, G. (2005). Radar soundings of the ionosphere of Mars. *Science*, *310*(5756), 1929–1933. https://doi.org/10.1126/science.1121868

Gurnett, D., Morgan, D., Duru, F., Akalin, F., Winningham, J., Frahm, R., … Barabash, S. (2010). Large density fluctuations in the Martian ionosphere as observed by the Mars Express radar sounder. *Icarus*, *206*(1), 83–94. https://doi.org/10.1016/j.icarus.2009.02.019

Halekas, J. S., Brain, D. A., Ruhunusiri, S., McFadden, J. P., Mitchell, D. L., Mazelle, C., … Jakosky, B. M. (2016). Plasma clouds and snowplows: Bulk plasma escape from Mars observed by MAVEN. *Geophysical Research Letters*, *43*, 1426–1434. https://doi.org/10.1002/2016GL067752

Halekas, J. S., Ruhunusiri, S., Harada, Y., Collinson, G., Mitchell, D. L., Mazelle, C., … Jakosky, B. M. (2016). Structure, dynamics, and seasonal variability of the Mars-solar wind interaction: MAVEN Solar Wind Ion Analyzer in-flight performance and science results. *Journal of Geophysical Research: Space Physics*, *121*, 547–578. https://doi.org/10.1002/2016JA023167

Harada, Y., Gurnett, D. A., Kopf, A. J., Halekas, J. S., Ruhunusiri, S., Lee, C. O., … Jakosky, B. M. (2017). Dynamic response of the Martian ionosphere to an interplanetary shock: Mars Express and MAVEN observations. *Geophysical Research Letters*, *44*. https://doi.org/10.1002/2017GL074897

Huang, C.-S., & Kelley, M. C. (1996). Nonlinear evolution of equatorial spread *F*: 1. On the role of plasma instabilities and spatial resonance associated with gravity wave seeding. *Journal of Geophysical Research*, *101*(A1), 283–292. https://doi.org/10.1029/95JA02211

Jordan, R., Picardi, G., Plaut, J., Wheeler, K., Kirchner, D., Safaeinili, A., … Bombaci, O. (2009). The Mars express MARSIS sounder instrument. *Planetary and Space Science*, *57*(14-15), 1975–1986. https://doi.org/10.1016/j.pss.2009.09.016

Keating, G. M., Bougher, S. W., Zurek, R. W., Tolson, R. H., Cancro, G. J., Noll, S. N., … Babicke, J. M. (1998). The structure of the upper atmosphere of Mars: In situ accelerometer measurements from Mars global surveyor. *Science*, *279*(5357), 1672–1676. https://doi.org/10.1126/science.279.5357.1672

Kelley, M. C., Makela, J. J., de La Beaujardière, O., & Retterer, J. (2011). Convective ionospheric storms: A review. *Reviews of Geophysics*, *49*, RG2003. https://doi.org/10.1029/2010RG000340

King, G. (1970). Spread-*F* on ionograms. *Journal of Atmospheric and Solar-Terrestrial Physics*, *32*(2), 209–221. https://doi.org/10.1016/0021-9169(70)90192-3

Kopf, A. J., Gurnett, D. A., DiBraccio, G. A., Morgan, D. D., & Halekas, J. S. (2017). The transient topside layer and associated current sheet in the ionosphere of Mars. *Journal of Geophysical Research: Space Physics*, *122*, 5579–5590. https://doi.org/10.1002/2016JA023591

Kopf, A. J., Gurnett, D. A., Morgan, D. D., & Kirchner, D. L. (2008). Transient layers in the topside ionosphere of Mars. *Geophysical Research Letters*, *35*, L17102. https://doi.org/10.1029/2008GL034948

Makela, J. J., & Otsuka, Y. (2012). Overview of nighttime ionospheric instabilities at low- and mid-latitudes: Coupling aspects resulting in structuring at the mesoscale. *Space Science Reviews*, *168*(1), 419–440. https://doi.org/10.1007/s11214-011-9816-6

Medvedev, A. S., & Yiğit, E. (2012). Thermal effects of internal gravity waves in the Martian upper atmosphere. *Geophysical Research Letters*, *39*, L05201. https://doi.org/10.1029/2012GL050852

Medvedev, A. S., Yiğit, E., Hartogh, P., & Becker, E. (2011). Influence of gravity waves on the Martian atmosphere: General circulation modeling. *Journal of Geophysical Research*, *116*, E10004. https://doi.org/10.1029/2011JE003848

Morgan, D. D., Gurnett, D. A., Kirchner, D. L., Fox, J. L., Nielsen, E., & Plaut, J. J. (2008). Variation of the Martian ionospheric electron density from Mars Express radar soundings. *Journal of Geophysical Research*, *113*, A09303. https://doi.org/10.1029/2008JA013313

Morgan, D. D., Witasse, O., Nielsen, E., Gurnett, D. A., Duru, F., & Kirchner, D. L. (2013). The processing of electron density profiles from the Mars Express MARSIS topside sounder. *Radio Science*, *48*, 197–207. https://doi.org/10.1002/rds.20023

Morschhauser, A., Lesur, V., & Grott, M. (2014). A spherical harmonic model of the lithospheric magnetic field of Mars. *Journal of Geophysical Research: Planets*, *119*, 1162–1188. https://doi.org/10.1002/2013JE004555

Němec, F., Morgan, D. D., Gurnett, D. A., & Brain, D. A. (2011). Areas of enhanced ionization in the deep nightside ionosphere of Mars. *Journal of Geophysical Research*, *116*, E06006. https://doi.org/10.1029/2011JE003804

Němec, F., Morgan, D. D., Gurnett, D. A., & Duru, F. (2010). Nightside ionosphere of Mars: Radar soundings by the Mars Express spacecraft. *Journal of Geophysical Research*, *115*, E12009. https://doi.org/10.1029/2010JE003663

Nielsen, E., Wang, X.-D., Gurnett, D. A., Kirchner, D. L., Huff, R., Orosei, R., … Picardi, G. (2007). Vertical sheets of dense plasma in the topside Martian ionosphere. *Journal of Geophysical Research*, *112*, E02003. https://doi.org/10.1029/2006JE002723

Opgenoorth, H., Dhillon, R., Rosenqvist, L., Lester, M., Edberg, N., Milan, S., … Brain, D. (2010). Day-side ionospheric conductivities at Mars. *Planetary and Space Science*, *58*(10), 1139–1151. https://doi.org/10.1016/j.pss.2010.04.004

Pfaff, R. F. (2012). The near-Earth plasma environment. *Space Science Reviews*, *168*(1), 23–112. https://doi.org/10.1007/s11214-012-9872-6

Press, W. H., Teukolsky, S. A., Vetterling, W. T., & Flannery, B. P. (1992). *Numerical recipes in C: The art of scientific computing*. New York: Cambridge University Press.

Reinisch, B. W., Abdu, M., Batista, I., Sales, G. S., Khmyrov, G., Bullett, T. A., … Rios, V. (2004). Multistation digisonde observations of equatorial spread F in South America. *Annales Geophysicae*, *22*(9), 3145–3153. https://doi.org/10.5194/angeo-22-3145-2004

Riousset, J. A., Paty, C. S., Lillis, R. J., Fillingim, M. O., England, S. L., Withers, P. G., & Hale, J. P. M. (2013). Three-dimensional multifluid modeling of atmospheric electrodynamics in Mars' dynamo region. *Journal of Geophysical Research: Space Physics*, *118*, 3647–3659. https://doi.org/10.1002/jgra.50328

Ruhunusiri, S., Halekas, J. S., McFadden, J. P., Connerney, J. E. P., Espley, J. R., Harada, Y., … Hasegawa, H. (2016). MAVEN observations of partially developed Kelvin-Helmholtz vortices at Mars. *Geophysical Research Letters*, *43*, 4763–4773. https://doi.org/10.1002/2016GL068926

Sales, G. S., Reinisch, B. W., Scali, J. L., Dozois, C., Bullett, T. W., Weber, E. J., & Ning, P. (1996). Spread *F* and the structure of equatorial ionization depletions in the southern anomaly region. *Journal of Geophysical Research*, *101*(A12), 26,819–26,827. https://doi.org/10.1029/96JA01946

Terada, N., Leblanc, F., Nakagawa, H., Medvedev, A. S., Yiğit, E., Kuroda, T., … Jakosky, B. M. (2017). Global distribution and parameter dependences of gravity wave activity in the Martian upper thermosphere derived from MAVEN/NGIMS observations. *Journal of Geophysical Research: Space Physics*, *122*, 2374–2397. https://doi.org/10.1002/2016JA023476

Tsunoda, R. T. (2010a). On equatorial spread *F*: Establishing a seeding hypothesis. *Journal of Geophysical Research*, *115*, A12303. https://doi.org/10.1029/2010JA015564

Tsunoda, R. T. (2010b). On seeding equatorial spread *F* during solstices. *Geophysical Research Letters*, *37*, L05102. https://doi.org/10.1029/2010GL042576

Tsunoda, R. T., Livingston, R. C., McClure, J. P., & Hanson, W. B. (1982). Equatorial plasma bubbles: Vertically elongated wedges from the bottomside *F* layer. *Journal of Geophysical Research*, *87*(A11), 9171–9180. https://doi.org/10.1029/JA087iA11p09171

Venkateswara Rao, N., Mohanamanasa, P., & Rao, S. V. B. (2017). Magnetically controlled density structures in the topside layer of the Martian ionosphere. *Journal of Geophysical Research: Space Physics*, *122*, 5619–5629. https://doi.org/10.1002/2016JA023545

Wang, J.-S., & Nielsen, E. (2003). Wavelike structures in the Martian topside ionosphere observed by Mars Global Surveyor. *Journal of Geophysical Research*, *108*(E7), 5078. https://doi.org/10.1029/2003JE002078

Wang, J.-S., & Nielsen, E. (2004). Evidence for topographic effects on the Martian ionosphere. *Planetary and Space Science*, *52*(9), 881–886. https://doi.org/10.1016/j.pss.2004.01.008

Withers, P. (2006). Mars Global Surveyor and Mars Odyssey Accelerometer observations of the Martian upper atmosphere during aerobraking. *Geophysical Research Letters*, *33*, L02201. https://doi.org/10.1029/2005GL024447

Withers, P. (2009). A review of observed variability in the dayside ionosphere of Mars. *Advances in Space Research*, *44*(3), 277–307. https://doi.org/10.1016/j.asr.2009.04.027

Withers, P., Bougher, S., & Keating, G. (2003). The effects of topographically-controlled thermal tides in the martian upper atmosphere as seen by the MGS accelerometer. *Icarus*, *164*(1), 14–32. https://doi.org/10.1016/S0019-1035(03)00135-0

Woodman, R. F. (2009). Spread F — An old equatorial aeronomy problem finally resolved?*Annales Geophysicae*, *27*(5), 1915–1934. https://doi.org/10.5194/angeo-27-1915-2009

Wright, J. W., Argo, P. E., & Pitteway, M. L. V. (1996). On the radiophysics and geophysics of ionogram spread *F*. *Radio Science*, *31*(2), 349–366. https://doi.org/10.1029/95RS03104

Yiğit, E., England, S. L., Liu, G., Medvedev, A. S., Mahaffy, P. R., Kuroda, T., & Jakosky, B. M. (2015). High-altitude gravity waves in the Martian thermosphere observed by MAVEN/NGIMS and modeled by a gravity wave scheme. *Geophysical Research Letters*, *42*, 8993–9000. https://doi.org/10.1002/2015GL065307